PHYSICAL REVIEW A VOLUME 23, NUMBER 5 MAY 1981

Soft-x-ray and x-ray ultraviolet radiation from high-density aluminum plasmas

D. Duston and J. Davis
Plasma Radiation Group, Naval Research Laboratory, Washington, D. C. 20375

(Received 8 August 1980)

Radiation emission over a wide range (5–5000 Å) of wavelengths in a high-density aluminum plasma has been studied theoretically. The atomic model includes explicit treatment of a large number of states and transitions characterizing the line emission from the Al III–Al XIII ions. The state populations are calculated using a set of atomic rate equations describing a plasma in collisional-radiative equilibrium. The ionization state of the plasma is calculated self-consistently with line and continuum radiation transport using a one-dimensional multicell structure for the plasma. A new radiation transport scheme has been implemented in this model based on probability of escape for both line and continuum photons. The total L- and K-shell radiation emission is described as a function of plasma temperature, density, and source size, and is compared to predictions made from corona and local thermodynamic equilibrium models. It is shown that over a wide range of plasma parameters, neither of these two limiting models accurately describes the plasma emission characteristics. Several line intensity ratios from L-shell lines are studied and shown to be useful diagnostic indicators of the plasma temperature and density. Finally, theoretical spectra are calculated and discussed in the context of their comparability with experimental spectra in order to make contact with real plasma radiation signatures and exploit the predictive capabilities of the model.

I. INTRODUCTION

The x-ray emission from high-density aluminum plasmas has received much attention in recent years due to interest in results from exploding wire experiments,[1,2] laser plasmas,[3,4] and particle beam-foil interactions.[5] Theoretical analysis of the radiation emission from these dense plasmas is useful for understanding both the plasma energetics and determination of plasma parameters from spectral diagnostics. Several models have been developed in an effort to understand various aspects of aluminum-plasma emissions, concentrating on K-shell ions,[6-10] and some L-shell[11] and M-shell[12] ions. In this study we include excited states from all ions of the K and L shells of aluminum as well as Al III in the M shell. In addition, the ionization dynamics and radiation-transport calculations are solved self-consistently for all included level populations producing line and continuum photons in a one-dimensional plasma model. The multicell aspect of this model also allows us to treat stationary plasmas in which there exists temperature and density gradients characteristic of imploding wire array plasmas.

This work will be presented in four sections. First, a detailed description of the level structure and rate coefficients employed in this model is presented along with a brief description of the ionization-radiation calculation as well as the radiation transport. Second, the gross characteristics of both the line and continuum radiation are studied as they vary with the plasma electron temperature, ion density, and plasma radius. The results are then compared with those obtained from local thermodynamic equilibrium (LTE) and corona models and define the plasma conditions necessary for the valid application of these models. Third, we explore the details of the bound-bound radiation spectrum to describe various line intensity ratios from the L-shell ions which can effectively be applied to diagnose plasma parameters in temperature regimes lower than that in which K-shell ions are abundant. Finally, in the fourth section we present theoretically generated emission spectrum and discuss, in detail, their implications with respect to plasma diagnostics. Although these calculations have been done for an aluminum plasma, the interplay between particle collisions and photon transport in determining level populations and radiation emission are expected to be typical of many dense plasmas. Therefore, we have attempted to be as general as possible in our analysis of the results, realizing that many of the trends occurring in this study will be typical of L-shell emission from other materials. Some features of the data will nevertheless be strongly dependent on the detailed rates and structure representative of aluminum in particular, and we have made an effort to point out these occurrences when not obvious.

II. ATOMIC MODEL

A. Level structure

Integral to any theoretical prediction of the radiation emission from a plasma which spans a significant temperature range in its evolution, is the detailed system of states included in the atomic model. In a previous work on K-shell

© 1981 The American Physical Society

emission,[6] we chose to include several higher-lying states whose emission was diagnostically useful but were not energetically significant. In this study, it was necessary to include many states for energetic purposes alone. Because of the smaller energy differences between ground and excited levels in L-shell ions as compared to those of the K shell, excited level populations constitute a nonnegligible fraction of the total population at ion densities typical of exploding wire plasmas, and one would like to include many levels in each ion to insure completeness of the radiative description. On the other hand, several criteria restrict the number of levels one can practically include in a model: (i) The availability of data for higher Rydberg members of L-shell aluminum ions, (ii) the unwieldiness of solving, self-consistently with radiation transport, a set of rate equations for several hundred levels, and (iii) time restrictions on computer runs to solve this large set of equations for a meaningfully extensive set of parameters. With these restrictions in mind, the number of levels to include per ion was decided upon after scanning several sources of x-ray ultraviolet (XUV) spectral data[13] and identifying the strongest lines. These spectra showed that $\Delta n = 0$ transitions of the forms $2s^2 2p^n - 2s2p^{n+1}$ and $2s2p^{n+1} - 2p^{n+2}$ were very evident in many of the shots, despite the high density of the plasmas. In addition, very few lines were identified above the principal quantum number 3 for all but the alkali-metal-like ions Al XI and Al III. We chose, therefore, to include, in addition to the ground states, the $n = 2$ and 3 levels in all ions in as complete a manner as possible, as well as a few higher-n states in the two alkali-metal ions. The complete level structure employed in this study is shown Table I along with the state energy (measured from ground). The energies of the states were taken from the level diagrams of Bashkin and Stoner[14] and the tables of Martin and Zalubas[15]; wavelengths of bound-bound transitions were taken from Ref. 14 and the tables of Kelly and Palumbo.[16]

In a previous study on the K-shell emission,[17] it was found that at high densities, many of the individual l states of a given n level may be in Boltzmann equilibrium with each other due to heavy particle collisions. Specifically, if the energy separation between level nl and nl' is small compared to the electron thermal energy, ion-ion collisions will cause the levels to equilibrate at densities lower than electron-ion collisions would.[17] Since the primary purpose of this investigation is to study high-density plasma radiation (typically, ion densities greater than 10^{18} cm^{-3}), the assumption has been made that many of the close-lying states have equilibrated and the ratio of their populations is given by the ratio of their statistical weights. The individual nl levels are then grouped as a single "degenerate" n level with the appropriate statistical weight. In addition, any rate populating this n level is an average (over initial states) of each rate populating the individual nl states. This method of treating levels of similar electron configurations, separated by only a few electron volts in energy, allows the model to carry a large number of excited levels while reducing computation time that would have been used calculating a known relationship between many of the levels. The brackets in Table I indicate the levels which were appropriately combined in our model.

B. Rate coefficients

With the exception of electron collisional excitation rate coefficients and spontaneous decay rates, the methods of calculating the various rate coefficients used in this study have been described in detail in previous papers,[6,18] and only brief reference will be made to these. Every state is coupled to the next (energetically) higher ground state by collisional ionization, photoionization, collisional recombination, and radiative recombination. The collisional-ionization rates are calculated by Seaton's prescription,[19] and the photoionization rates are calculated in the hydrogenic approximation[20] using effective free-bound Gaunt factors.[21] Collisional and radiative recombination rates are then calculated as the detailed balance of these. In addition, adjacent ground states are coupled by dielectronic recombination[22] found by summing capture rates over a manifold of states above the ionization limit which then decay via cascade to the ground state.

Excited levels of a given ion are coupled to other selected excited levels and the ground state by electron collisional excitation and deexcitation, stimulated emission and absorption, and spontaneous radiative decay. In the K-shell ions, Al XII and Al XIII, and in Al XI, the collisional couplings are complete, including forbidden and spin-flip transitions as well as those which are dipole allowed. For Al XIII, the Coulomb-Born approximation[23] was used, while a distorted-wave calculation with exchange[24] was used to calculate the coefficients for Al XI and Al XII. Comparisons of these two methods have been made for several transitions in Al XIII (Ref. 17), and excellent agreement was obtained.

The prohibitively large number of levels to be collisionally coupled in the remaining ions pre-

TABLE I. Atomic level structure for aluminum included in the collisional-radiative equilibrium model (brackets indicate levels which were grouped together in the calculation).

Level	Energy (eV)
Al	
$1s^22s^22p^63s^23p\,^2P$	0.0
Al II	
$1s^22s^22p^63s^2\,^1S$	0.0
Al III	
$1s^22s^22p^63s\,^2S$	0.0
$3p\,^2P$	6.675
$3d\,^2D$	14.377
$4s\,^2S$	15.64
$4p\,^2P$	17.815
$4d\,^2D$	20.555
$4f\,^2F$	20.782
Al IV	
$1s^22s^22p^6\,^1S$	0.0
$2p^53s\,^3P$	76.68
$2p^53s\,^1P$	77.45
$2p^53p\,^1D$	85.02
$2p^53p\,^3P$	85.32
⎧ $2p^53d\,^3P$	94.23
⎩ $2p^53d\,^1P$	95.57
$2p^53d\,^3D$	95.14
$2p^54s\,^3P$	99.47
$2p^54s\,^1P$	99.93
Al V	
$1s^22s^22p^5\,^2P$	0.0
$2s2p^6\,^2S$	44.49
$2s^22p^43s\,^2P$	94.86
$2s^22p^43s\,^2D$	98.77
$2s^22p^43s\,^2S$	104.38
⎧ $2s^22p^4(^3P)3d\,^2F$	114.28
⎨ $2s^22p^4(^3P)3d\,^2D$	114.82
⎩ $2s^22p^4(^3P)3d\,^2P$	115.01
⎧ $2s^22p^4(^1D)3d\,^2S$	119.08
⎪ $2s^22p^4(^1D)3d\,^2P$	119.17
⎪ $2s^22p^4(^1D)3d\,^2D$	119.39
⎩ $2s^22p^4(^1D)3d\,^2F$	119.44
Al VI	
$1s^22s^22p^4\,^3P$	0.0
⎧ $2s^22p^4\,^1D$	5.104
⎩ $2s^22p^4\,^1S$	10.937
$2s2p^5\,^3P$	40.20
$2s2p^5\,^1P$	55.97
⎧ $2s^22p^33s\,^3S$	113.21
⎨ $2s^22p^33s\,^3D$	119.16
⎩ $2s^22p^33s\,^3P$	123.21
⎧ $2s^22p^33s\,^1D$	120.31
⎩ $2s^22p^33s\,^1P$	124.39
$2s^22p^3(^4S)3d\,^3D$	133.85
⎧ $2s^22p^3(^2D)3d\,^3F$	140.55
⎪ $2s^22p^3(^2D)3d\,^3D$	140.63
⎪ $2s^22p^3(^2D)3d\,^3P$	141.50
⎩ $2s^22p^3(^2D)3d\,^3S$	141.97
⎧ $2s^22p^3(^2D)3d\,^1P$	140.86
⎨ ^1D	141.57
⎩ ^1F	142.56
⎧ $2s^22p^3(^2P)3d\,^3P$	144.43
⎨ ^3F	144.80
⎩ ^3D	144.95
⎧ $2s^22p^3(^2P)3d\,^1D$	145.14
⎨ ^1P	145.30
⎩ ^1F	145.56
Al VII	
$1s^22s^22p^3\,^4S$	0.0
$2s^22p^3\,^2D$	7.73
^2P	11.75
$2s2p^4\,^4P$	34.92
⎧ ^2D	47.84
⎨ ^2S	56.17
⎩ ^2P	59.35
$2p^5\,^2P$	91.39
$2s^22p^23s\,^4P$	142.53
$3s\,^2D$	148.58
⎧ $2s^22p^2(^3P)3d\,^4D$	164.15
⎩ ^4P	164.59
⎧ $2s^22p^2(^3P)3d\,^2P$	163.35
⎨ ^2F	164.50
⎩ ^2D	166.85
⎧ $2s^22p^2(^1D)3d\,^2F$	169.66
⎪ ^2D	170.02
⎪ ^2P	171.15
⎩ ^2S	171.97
Al VIII	
$1s^22s^22p^2\,^3P$	0.0
⎧ $2s^22p^2\,^1D$	5.97
⎩ $2s^22p^2\,^1S$	11.93
$2s2p^3\,^5S$	16.55
⎧ $2s2p^3\,^3D$	32.51
⎨ ^3P	38.33
⎩ ^3S	50.11
⎧ ^1D	49.22
⎩ ^1P	55.12
$2p^4\,^3P$	75.58
⎧ ^1D	80.25
⎩ ^1S	91.56
⎧ $2s^22p3d\,^3F$	182.10
⎨ ^3D	184.21
⎩ ^3P	184.87
⎧ ^1D	182.50
⎨ ^1F	187.12
⎩ ^1P	187.23

TABLE I. (*Continued*)

Level	Energy (eV)	Level	Energy (eV)
$2s2p^2(^2D)3s\ ^3D$	196.57	$2p3s\ ^1P$	259.36
$2s2p^2(^4P)3d\ ^5P$	202.37	$2p3p\ ^1P$	259.73
$2s2p^2(^4P)3d\ ^3P$	202.70		266.38
^3F	203.93	$2p3p\ ^1P$	265.53
^3D	206.46	^1F	271.89
$2s2p^2(^2D)3d\ ^3F'$	215.00	^1P	272.73
^3D	216.01		
^3P	216.81	Al XI	
^3S	218.47	$1s^22s\ ^2S$	0.0
		$2p\ ^2P$	22.30
Al IX		$3s\ ^2S$	250.51
$1s^22s^22p\ ^2P$	0.0	$3p\ ^2P$	256.64
$2s2p^2\ ^4P$	18.236	$3d\ ^2D$	258.93
^2D	32.205	$4s\ ^2S$	335.47
^2S	41.25	$4p\ ^2P$	338.07
^2P	44.14	$4d\ ^2D$	339.02
$2p^3\ ^4S$	57.04	$4f\ ^2F$	339.10
^2D	64.49	$5s\ ^2S$	374.10
^2P	72.58	$5p\ ^2P$	375.64
$2s^23s\ ^2S$	186.11	$5d\ ^2D$	376.14
$2s^23p\ ^2P$	195.11	$5f\ ^2F$	376.16
$2s^23d\ ^2D$	203.62	$5g\ ^2G$	376.17
$2s2p3d\ ^4P$	223.94	$6s\ ^2S$	395.26
^4D	222.94	$6p\ ^2P$	395.96
$2s2p(^3P)3d\ ^2D$	223.27	$6d\ ^2D$	396.31
^2F	227.28	$6f\ ^2F$	396.32
^2P	228.26	$6g\ ^2G$	396.36
$2s2p(^1P)3d\ ^2F$	239.67	$6h\ ^2H$	396.38
^2D	240.98	$1s2p^2\ ^2D$	1596.70
^2P	242.36		
$2s2p4d\ ^4D$	279.46	Al XII	
^4P	279.79	$1s^2\ ^1S$	0.0
		$1s2s\ ^3S$	1575.06
Al X		$1s2p\ ^3P$	1588.5
$1s^22s^2\ ^1S$	0.0	$1s2s\ ^1S$	1589.03
$2s2p\ ^3P$	19.67	$1s2p\ ^1P$	1598.37
$2s2p\ ^1P$	37.26	$n=3$, triplet	1866.08
$2p^2\ ^3P$	50.59	$n=3$, singlet	1868.63
$2p^2\ ^1D$	55.76	$n=4$, singlet	1963.89
$2p^2\ ^1S$	68.66	$n=5$, singlet	2006.47
$2s3s\ ^3S$	230.09		
$2s3p\ ^3P$	239.16	Al XIII	
$2s3d\ ^3D$	243.77	$n=1$, doublet	0.0
$2s3s\ ^1S$	233.64	$n=2$, doublet	1728.71
$2s3p\ ^1P$	238.53	$n=3$, doublet	2048.57
$2s3d\ ^1D$	247.02	$n=4$, doublet	2160.66
$2p3s\ ^3P$	255.06	$n=5$, doublet	2212.31
$2p3p\ ^3D$	261.02		
^3S	262.81		
^3P	264.06		
$2p3d\ ^3D$	268.10		
^3P	269.14		

cluded the indiscriminate use of the distorted-wave calculation for these transitions. Instead, a calculation employing the semiclassical impact-parameter method[25] with thermally averaged Gaunt factors[26] was used to couple levels between which electric-dipole transitions are allowed, while forbidden transitions were neglected. When dipole oscillator strengths, required by the impact-parameter code, were not available, a Bates-Damgaard calculation[27] was used to generate them.

Many of the ions contain excited levels from several spin systems and it was necessary to collisionally couple these systems (usually between the lowest-lying excited state in the system and the ground state); the distorted-wave calculation was used for these transitions to take account of the spin flip. If these couplings are not included, the state populations in the spin system not coupled to the lower ground state are found to float somewhat at low electron densities, being coupled only to the ground state above by collisional ionization and radiative recombination. While collisional ionization may be the dominant *depopulating* mechanism for these states at low densities, collisional excitation from the ground state dominates over radiative recombination as the main *populating* process; hence, if these collisional excitation rates are not included, incorrect populations for these states will be predicted by the model.

Dipole oscillator strengths and spontaneous radiative decay rates for the L-shell ions were extracted from several sources. The very complete tabulation by Lindgård and Nielsen[28] was the source of these rates for lithiumlike Al XI and sodiumlike Al III. Many of the oscillator strengths describing the transitions $2s^2 2p^n - 2s2p^{n+1}$ and $2s2p^{n+1} - 2p^{n+2}$ for berylliumlike Al X through oxygenlike Al VI were found in the calculations by Fawcett.[29] The following references were also consulted as sources for oscillator strengths: Martin and Simons[30] for Al X, Shamey[31] and Weiss[32] for Al IX, McIntyre *et al.*[33] for Al VIII, Buchet and Buchet-Poulizac[34] for Al V – VII, Kernahan *et al.*[35] for Al III–VII, Mewe[36] for Al V, and Shorer[37] and Loginov and Gruzdev[38] for Al IV. Finally, the tables of transition probabilities by Wiese *et al*[39] were used for many of the L-shell f values not located in the above sources. As stated earlier, all oscillator strengths not contained in the references were generated from a Bates-Damgaard calculation.

A brief discussion at this point about the effect of neglecting forbidden transitions in the L-shell ions is warranted. At low density, this is a good approximation if the radiation emission is the quantity one is most concerned with. At these densities, the plasma is in the coronal regime and excited states are populated predominantly by electron collision from the ground state. Consequently, only low-lying $n=2$ levels will have significant populations and the bulk of the line radiation will be due to transitions from these states. Since almost all of the transitions involving a $2s-2p$ excitation are dipole allowed, the $n=2$ populations and hence the radiation will be calculated accurately. Since many of the $n \geq 3$ levels are forbidden in their coupling to the ground state, their populations may not be as accurate, but the radiation from these states is negligible at low densities. At high densities, collisional ionization and recombination between excited states and the next higher ground state dominate the redistribution of the populations among the excited states; since these rates are included in the model, all population densities are accurately determined in the LTE regime. The collisional-radiative regime between corona and LTE is where collisional excitation processes are most important in determining the populations of states with $n \geq 3$. Although forbidden transitions will definitely affect the populations of and radiation from these levels, we place the error in populations due to the neglect of these rates at a maximum of a factor of 2 and an uncertainty of at most 50% in the total radiation emission (based on our previous work with collisional couplings in the aluminum K shell). The inclusion of forbidden transitions and their effect on the L-shell line emission will be the subject of a future study.

C. Ionization dynamics and radiation transport

The scheme for solving the ionization dynamics of an equilibrium plasma has been described in detail in earlier work.[6] Briefly, an atomic rate equation of the form

$$\frac{dN_i}{dt} = \sum_j W_{ji} N_j - \sum_j W_{ij} N_i \tag{1}$$

can be written for each ground and excited state included in the model, where W_{ji} is a rate for populating state i, and W_{ij} is a rate for depopulating state i. In this study, the approximation is made that the plasma radiation pulse is short compared to characteristic hydrodynamic time scales, and hence, state populations are constant during the duration of the pulse. This allows for a steady-state solution and the time derivative can be set to zero in Eq. (1). In addition, no hydrodynamic equations are as yet solved together with the rate equations; thus, the solution to the set of equations (1) represents a plasma frozen in space and time at, for example, the point of peak plasma emission.

The radiation transport employed here represents an improvement on our phenomenological frequency-diffusion technique reported on earlier,[6,17] and is based on a calculation of the probability of escape of photons born in the plasma. The probability that photons born in a given zone of the plasma and reabsorbed in a different zone (or allowed to escape to the detector) is calculated, taking into account both stimulated emission and stimulated absorption processes. These probabilities are calculated assuming that the line emission profile is a Voigt and, therefore, both Doppler and collisional broadening contribute to the line width.

The probability of escape for a Voigt line profile is defined by Hummer[40] and is given by

$$p_e \simeq \frac{2}{3}\left(\frac{a_{ij}}{\tau_0}\right)^{1/2}, \tag{2}$$

where τ_0 is the line-center optical depth and a_{ij} is the Voigt damping parameter defined by

$$a_{ij} = \frac{\sum_k A_{ik} + \sum_k X_{ik} + \sum_k A_{jk} + \sum_k X_{jk}}{4\pi\Delta\nu_D}. \tag{3}$$

Here, A and X represent all radiative and collisional rates depopulating the upper level i and the lower level j of the transition, while $\Delta\nu_D$ is the Doppler width of the line

$$\Delta\nu_D = \left(\frac{2kT_i}{Mc^2}\right)^{1/2}\nu_0, \tag{4}$$

where T_i is ion temperature, M is ion mass, and ν_0 is the photon frequency at line center. Using the expression in Eq. (2), the probability that a photon emitted in cell m will traverse, unabsorbed, to a cell boundary can be calculated. Thus, using the difference of such probabilities, one can determine the probability that a photon emitted in zone m will be absorbed in zone m'. By calculating zone-to-zone coupling coefficients, $C(m,m')$, in this way for each emission line one computes the probability of escape from zone m by

$$P_e(m) = 1 - C(m,m), \tag{5}$$

where $C(m,m)$ is the coupling coefficient relating the probability that a photon emitted in zone m will be reabsorbed in zone m. The photon pumping rate in zone m due to photons emitted in other zones and absorbed in zone m is then given by

$$R_{\text{pump}} = \frac{\sum_{m' \neq m} N^*(m') A C(m',m) \Delta V(m')}{\Delta V(m)}, \tag{6}$$

where N^* is the density of the upper state of the transition, A is the radiative decay rate, ΔV is the zonal volume, and the coupling coefficients $C(m',m)$ contain terms accounting for both stimulated absorption (photoexcitation) and stimulated emission. The quantities calculated in Eqs. (5) and (6) are employed in the atomic rate equations since the reabsorption of photons can significantly alter the ionization-state and excited-state distributions in the plasma.[6] Finally, we define the probability of escape of a line photon from zone m to the spectrometer

$$P_{\text{esc}}(m) = 1 - \sum_{m'} C(m,m') \tag{7}$$

and the line intensity that exits the plasma

$$I_{\nu_0} = \sum_m N^*(m) A P_{\text{esc}}(m) h\nu_0 \Delta V(m). \tag{8}$$

In a time-dependent calculation, I_{ν_0} would be integrated in time to describe the temporal evolution of the spectral line as the state densities and opacity of the plasma change.

While this method is very accurate for plasmas which are homogeneous in density and temperature, the treatment of plasmas with gradients by this method warrants some discussion. The exact expression for the photon escape probability involves an integral over both the emission and absorption profile functions, where the absorption profile (as well as the emission profile) is dependent on the temperature and density conditions across the plasma. For a plasma with temperature and density gradients, no account is taken of the changing absorption profile when the analytic expression given by Eq. (2) for the Voigt profile is used. Therefore, it is necessary to place some bounds on the error that might be incurred in calculating the probabilities in this way for an inhomogeneous plasma.

The width of a Voigt-broadened emission line is proportional to $(a\tau_0)^{1/2}$; hence, under the assumption of complete frequency redistribution, the absorption profile varies similarly. Since the optical depth at line center is explicitly calculated across each plasma zone before implementation in Eq. (2), the absorption width will be in error approximately to the degree that the root of the damping parameter a from the emitting zone to the absorbing zone varies. Now, the Voigt damping parameter is proportional to the sum of the radiative and collisional rate coefficients divided by the square root of the ion temperature [see Eq. (3)], hence, a is dependent on both density and temperature.

First, let us assess the effect of a temperature gradient on a. In many cases, particularly at lower densities, the radiative broadening dominates, and a varies only by $T_i^{1/2}$. Since an ion species exists in a plasma in significant fraction over, at most, a range of temperatures which vary by a factor of 3 (if the ion partial fraction decreases significantly, the optical depth becomes small and self-absorption is negligible), the damping parameter will change by at most a factor of 1.7 over this range. If the collisional broadening dominates a, by how much can it vary while the ion species of interest is still a major plasma component? The collisional rates which dominate the broadening usually couple close-lying levels, and the rate coefficients describing this coupling are usually in a temperature range above threshold; thus, they are decaying slowly. Over the significant temperature range discussed above, these rate coefficients rarely vary by more than a factor of 2 (as an example, the Al XI $2s-2p$ collisional excitation rate coefficient is 7.6×10^{-9} and 4.4×10^{-9} $\mathrm{cm}^3/\mathrm{sec}$ at 70 and 400 eV, respectively). Thus, the damping factor varies by, at most, this factor also. Hence, we determine that the existence of a temperature gradient can cause a meaningful difference of less than a factor of 2 in the emission and absorption widths for a Voigt profile.

Now, we assess the effect of a density gradient on a. An individual ion species can often comprise a significant fraction of the plasma ion distribution over several orders of magnitude change in density. Since a is proportional to collisional broadening when it dominates over radiative broadening, the conclusion is that every order of magnitude change in density from emission to absorption zone will be manifested as a change in the absorption width of about a factor of 3.

Numerical integrations of the exact expression for the Voigt profile to yield escape probabilities show that when the emission and absorption widths differ by a factor of 10, the probabilities will change from about 15% at $\tau_0=1$ to about 100% at $\tau_0=1000$ in relation to those calculated using *identical* emission and absorption widths. This model is intended to be applied to describe laboratory plasmas in which the density range typically changes by less than an order of magnitude over the plasma radius; however, rarely is a single ion species dominant over the entire range. Thus, in the worst case, when the profile is dominated by collisional broadening and a single ion species is strongly populated over a density gradient of 2 orders of magnitude, we can expect about a factor of 2 error in the probability of escape at large optical depths and much less at smaller τ_0's. When any of the above conditions is relaxed, of course, the error in the probability calculated by the model becomes smaller. Since the optical depths of strong lines in laboratory plasmas of interest rarely exceeds 500, we feel that this model yields an acceptable representation of radiation transport in inhomogeneous plasmas with very sharp gradients and an accurate representation over most of the parameter space to be investigated where gradients are somewhat flatter. However, it is the responsibility of the investigator to ascertain the regions of validity for each particular case.

A more detailed discussion of the method of calculating the coupling coefficients and the probability of escape transport technique can be found in the work of Apruzese *et al.*[41] In addition to transporting line photons, we have developed a method for transporting bound-free continuum photons as well. Using the photoionization cross sections calculated by a method described earlier, a probability of escape for photons originating from radiative recombinations is calculated based on the recombination edge profile and implemented in the rate equations in a way similar to that for the line photons. A detailed description of this method will be described in a following work.

III. RADIATION POWER IN PLASMAS

The main emphasis of this study is to quantify both the gross and detailed features of the radiation emission from the L-shell ions of dense aluminum plasmas. Previously, it was necessary to characterize the gross nature of the emission by either a corona model in the low-density limit, or an LTE model in the high-density limit. In this section, we present collisional-radiative equilibrium (CRE) results from a study of the line and continuum radiation as they vary with plasma temperature, density, and size. In addition, comparisons are made between predictions of this CRE calculation and the other two limiting models to establish regions of validity for their application.

In order to assess the collisional properties of the plasma and allow for a more equitable comparison between models, a study of the total line emission as a function of temperature and ion density was conducted with the initial assumption that the plasma was optically *thin*. The results are shown in Fig. 1, where the total bound-bound emission power coefficient (power density divided by electron density divided by ion density) is plotted as a function of electron temperature for various ion densities from $10^{11}-10^{23}$ cm^{-3}. Plotting the power coefficient allows one to easily discern the departure from corona equilibrium, since that model predicts a coefficient which is independent of density. The radiation from L-shell ions is seen in Fig. 1 to peak at about 60 – 120 eV while the K-shell emission maximizes at 1 keV. The curves for 10^{11} and 10^{13} cm^{-3} are identical, indicating that the plasma can truly be described by a corona model at those densities. Deviations from coronal equilibrium become noticeable above 10^{15} cm^{-3} for L-shell radiation and above 10^{19} cm^{-3} for K-shell radiation. At low densities, the maximum radiative emission at the L shell exceeds that of the K shell by an order

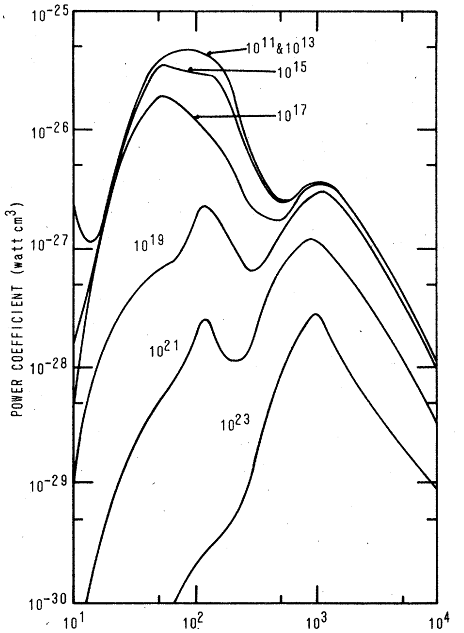

FIG. 1. Total line emission power coefficient vs electron temperature for densities from 10^{11}–10^{23} ions/cm^3 (optically thin approximation).

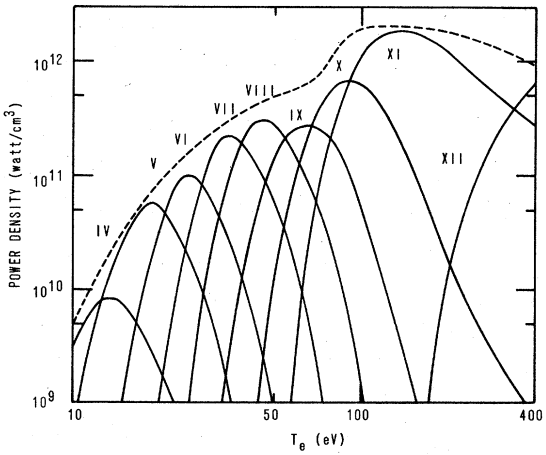

FIG. 2. Ionic line emission power densities vs electron temperature for a plasma at 10^{19} ions/cm^3 (optically thin approximation); total L-shell emission is also shown (broken line).

of magnitude, while at high densities, the K-shell radiation is much stronger. This is due to the increase in electron collisional quenching of L-shell photons as the density is increased and the L-shell ion states tend toward LTE. In fact, at 10^{23} ions/cm^3, at temperatures below 1 keV, the L-shell peak disappears completely, leaving a functional dependence suggestive of the power radiated by a blackbody, viz.,

$$P=\sigma T^4\,, \qquad (9)$$

where σ is the Stefan-Boltzmann constant and T is plasma temperature. The deviation from corona equilibrium for the K shell first appears at about 10^{19} ions/cm^3; this occurs at a much higher density for the K shell because typical energy separations between ground and excited states in the K shell are much larger, and hence, collisional deexcitation rates are much smaller than those for L-shell ions. (The corona approximation is no longer valid when collisional deexcitation becomes comparable to radiative decay in depopulating excited states).

The curves shown in Fig. 1 are, of course, due to the manifold of L- and K-shell ions emitting line radiation which is peaked at temperatures corresponding to roughly the peak in their ground-state abundances. The individual ionic contributions to the total line emission are shown in Fig. 2, where radiated power density versus T_e (electron temperature) for an optically thin plasma at 10^{19} ions/cm^3 is plotted. Notice that the boronlike Al IX peak falls somewhat below the Al VIII peak disrupting what was a monotonic increase in peak intensities with increasing ionic charge. This could be due to some inherent atomic structure differences such as a reduction in intensity as a closed subshell is attained, a possible error in an oscillator strength, or some level structure being left out of the model. Since the peak would need an increase of about 50% to bring it in line with the ionic trend, it is possible that the radiation from some $n=3$ states not included in the model could account for the difference. According to model predictions, the strongest radiating lines at 70 eV (Al IX peak temperature) in Al IX are $2s^22p(^2P)-2s^23s$, $-3p$, $-3d$ (doublet), $2s2p^2(^4P)-2s2p3d(^4P,^4D)$, and $2s^22p(^2P)-2s2p^2(^2S,^2P,^2D)$, in that order. The $2s2p3s$, $-3p$ (quartet) states were not included, but it is possible that they could have accounted for a significant portion of the Al IX emission due to their transitions to the $2s2p^2(^4P)$ level.

It was started earlier that in the coronal regime the bulk of the plasma line radiation emanating from the L-shell ions is due to $\Delta n=0$ transitions within the $n=2$ states. To illustrate how that changes as density increases, the individual line power densities from Al VIII (carbonlike) are shown versus T_e for an optically thin plasma at 10^{19} cm^{-3} in Fig. 3. The transitions in Al VIII shown in this figure are listed in Table II along with their approximate wavelengths. Note that while $n=2$ transitions still dominate, a large portion of the radiation now comes from decays from $n=3$ levels. The peak intensities for these

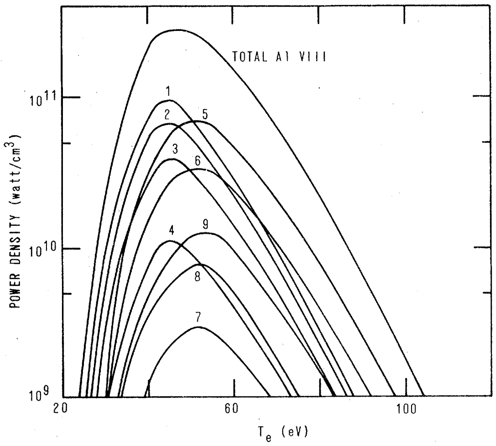

FIG. 3. Individual line emission power densities for Al XIII (carbonlike) vs electron temperature for a plasma at 10^{19} ions/cm^3 (optically thin approximation). See Table II for line identifications.

transitions occur at slightly higher temperatures than the $n=2$ transitions due to their larger excitation energies. The extent to which the higher Rydberg states contribute to the total ionic line emission at high plasma densities can seriously affect the validity of the atomic model. If not enough level structure is included in the model, the theoretical calculation may seriously underestimate the gross radiation features. As an example, one would probably assume that $n=4$ and 5 levels would be important at densities above $\sim 10^{20}$ cm^{-3} based on Fig. 3; hence, the two curves in Fig. 1 for ion densities of 10^{21} and 10^{23} cm^{-3} could be in error due to the omission of these and even higher levels. This would, in fact, be the case if it were not for lowering of the ionization potential in dense plasmas. Using the method prescribed by Griem,[42] the ionization lowering was determined for carbonlike Al VIII in a 50 - eV plasma. At an ion density of 10^{19} cm^{-3}, the lowering is only about 5.0 eV; however, at 10^{21} cm^{-3}, it is nearly 45.0 eV and the reduced ionization limit falls approximately 10 eV above several of the $n=4$ excited states in this ion, pushing higher-energy states into the continuum. While these estimates are only approximate, it is doubtful that gross errors are present in the radiation calculations. Moreover, it is found that lithiumlike Al XI is the strongest L-shell radiator above 10^{19} cm^{-3}, peaking at about 100 eV, and excited levels up to $n=6$ have been included for this ion to assure approximately correct calculation of the peak intensity at high densities (at 10^{21} ions/cm^3 and 100 eV, the calculated ionization potential of Al XI lies just above the $n=5$ level).

TABLE II. Transitions within the carbonlike Al VIII ion included in the CRE model (see Fig. 3 for power densities).

Key	Transition
II.1	$2s^22p^2(^3P)-2s2p^3(^3S,{}^3P,{}^3D)$
II.2	$2s^22p^2(^1S,{}^1D)-2s2p^3(^1P,{}^1D)$
II.3	$2s2p^3(^3S,{}^3P,{}^3D)-2p^4(^3P)$
II.4	$2s2p^3(^1P,{}^1D)-2p^4(^1S,{}^1D)$
II.5	$2s^22p^2(^3P)-2s^22p3d(^3P,{}^3D)$
II.6	$2s^22p^2(^1S,{}^1D)-2s^22p3d(^1P,{}^1D,{}^1F)$
II.7	$2s2p^3(^3P,{}^3D)-2s2p^2(^2D)3s(^3D)$
II.8	$2s2p^3(^5S)-2s2p^23d(^5P)$
II.9	$2s2p^3(^3P,{}^3D)-2s2p^2(^4P)3d(^3P,{}^3D,{}^3F)$ $-2s2p^2(^2D)3d(^3S,{}^3P,{}^3D,{}^3F)$

As plasma density increases, the level populations and, thus, the radiation emission approach values that would be predicted by an LTE model. This trend is illustrated in Fig. 4, where we have used an LTE calculation with the identical level structure as in our CRE model to predict the optically thin line emission; a comparison is made with the CRE results for three ion densities. At 10^{21} ions/cm^3 the L-shell line emission is very nearly in LTE while the K shell is not. At 10^{23}

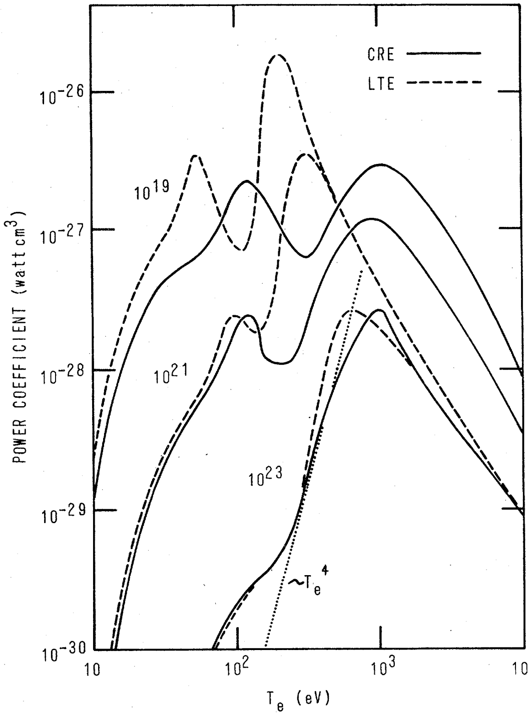

FIG. 4. Comparison of CRE (solid) and LTE (broken) line emission power coefficients for plasma densities from 10^{19}–10^{23} ions/cm^3 (optically thin approximation).

ions/cm^3, the L shell is in LTE and the K shell shows only small differences from LTE. An approximate hydrogenic formula[42] can be used to determine the density at which excited states go into LTE (in cm^{-3}),

$$Ne \geq 9\times10^{17}\left(\frac{\Delta E}{E_H}\right)^3\left(\frac{T_e}{E_H}\right)^{1/2}, \qquad (10)$$

where ΔE is the transition energy and E_H is the ionization potential of hydrogen. Using the $n=3$ state of Al XI at 120 eV yields an electron density of 1.8×10^{22} cm^{-3} or an ion density of $\sim2\times10^{21}$ cm^{-3}, which gives very reasonable agreement with the result in Fig. 4, at 120 eV.

In the interest of comparison with corona and LTE models, CRE results have been presented for optically thin plasmas only. Photon reabsorption, however, will play a more important role for L-shell line emission than for the K shell in dense laboratory plasmas. In order to study the effect of photoexcitation and stimulated emission on the radiation, the plasma size was varied for a number of calculations, since the photoexcitation rates are dependent on the optical depth which is, in turn, dependent on the plasma physical extent. Shown in Fig. 5 is the bound-bound power density versus T_e for a plasma at 10^{19} ions/cm^3 and a radius which varies from 50 to 5000 μm (the thin curve is also plotted). Note that at these parameters, the K shell is only slightly affected by opacity while the L-shell emission is reduced at peak T_e (120 eV) by factors of $\frac{1}{3}$, $\frac{1}{6}$, and $\frac{1}{9}$ of the thin result as the radius increases by an order of magnitude. Since the optical depth is also proportional to the population density of the lower state of the transition, it is expected that these opacity effects will be magnified at higher densities, while at lower densities, the emission will tend toward the optically thin values.

In addition to line photons, the radiation from free-bound transitions (due to radiative recombination) is also transported. The effects of opacity on the continuum are illustrated in Fig. 6 where the continuum power density is shown versus T_e for the same plasma parameters as in Fig. 5. Note that in the region of L-shell emission the effect by which the plasma experiences radiation attenuation by opacity effects appears to be reversed. Since reabsorption and transport of *line* photons results in strong optical pumping of the excited-state populations, the increase in ground-state populations via collisional ionization results in a subsequent increase in radiative recombination photons which more than compensates for the attenuation of continuum photons by photoionization processes (photoionization is almost negligible at these plasma parameters). Hence, the continuum radiation power density, being strongly tied to the excited-state densities, increases as the radius of the plasma increases. This anomalous behavior is, however, strongly density dependent, and photon attenuation by photoionization processes will overtake the pumping effects described above as the plasma density rises. Also notice, upon comparison, that while K-shell line emission dominates over continuum emission by about a factor of 5, the continuum radiation from L-shell ions is comparable to or exceeds the line photons for laboratory-size plasmas at this density.

Having examined both bound and continuum contributions to the emission individually, we are now in a position to understand the *total* radiation emission characteristics, shown in Fig. 7, for identical plasma parameters as in Figs. 5 and 6.

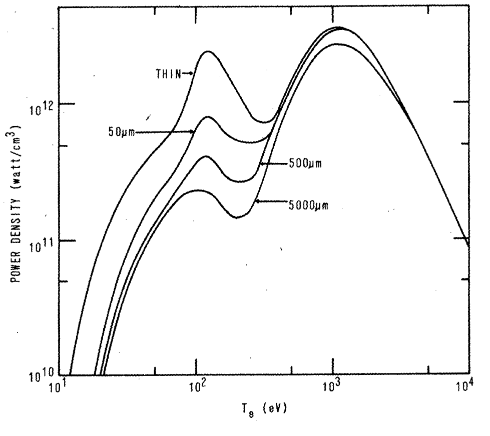

FIG. 5. Total line emission power densities (with opacity effects) for a plasma cylinder at 10^{19} ions/cm^3 and radii from 50–5000 μm.

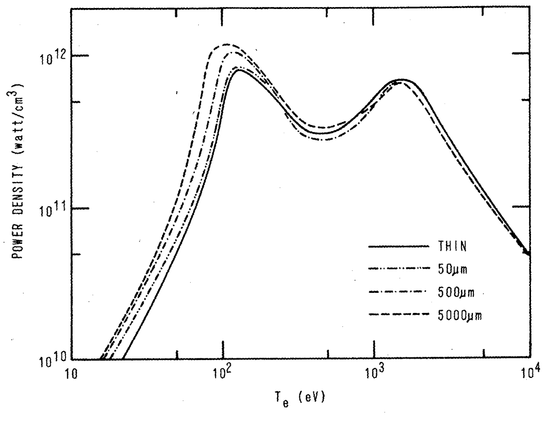

FIG. 6. Total free-bound continuum emission power densities (with opacity effects) for a plasma cylinder at 10^{19} ions/cm^3 and radii from 50–5000 μm.

The most striking feature is the relatively small difference between total radiated power density for the 50, 500, and 5000 μm plasmas over all ranges of temperature at 10^{19} ions/cm^3. Only the optically thin approximation differs significantly, and only by a factor of 6 at the L-shell peak at 130 eV. A consideration of the behavior of line and continuum radiation from the previous two figures shows quite clearly the compensating effect of their contributions.

An approximation that is often used to characterize the emission from dense plasmas is the black-body emission rate, given by Eq. (9). Converting the flux to a power density, the black-body (BB) radiation emission is also plotted in Fig. 7 for the three relevant plasma radii. While the slope of the BB curves is similar to the CRE curves, large quantitative errors result from using this approximation to describe a plasma at 10^{19} ions/cm^3 except at temperatures lower than 15 eV for the 5000-μm plasma. It is conceivable, however, that one could use the BB approximation to describe the plasma emission by employing a BB temperature *lower* than the actual plasma electron temperature. For example, a black-body radiation function would approximately describe the emission of a 5000-μm plasma at 10^{19} cm^{-3} if the BB temperature used was about half of the actual temperature; factors of about $\frac{1}{3}$ and $\frac{1}{6}$ could be also used for the 500- and 50-μm plasmas, respectively. The approximation, of course, is only good up to the temperature where the L-shell radiation peaks, since, at 10^{19} cm^{-3}, the K shell is substantially removed from the LTE state which Eq. (9) characterizes.

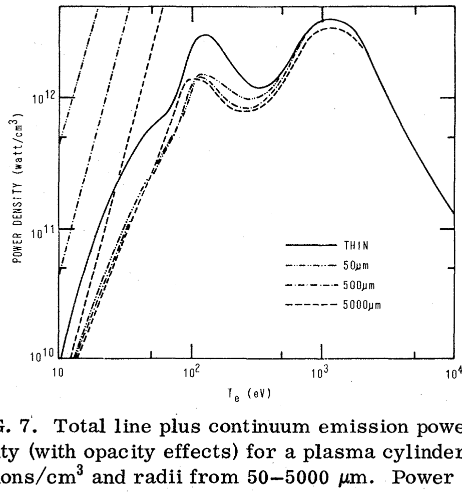

FIG. 7. Total line plus continuum emission power density (with opacity effects) for a plasma cylinder at 10^{19} ions/cm^3 and radii from 50–5000 μm. Power density from similar plasmas in the black-body limit are also shown (straight curves in upper left).

The approximation is still quite crude at 10^{19} ions/cm^3 because the slope of the BB is steeper than the CRE curve. To illustrate the trend toward black-body emission as density increases, a curve has been drawn in Fig. 4 (dotted line) which represents the T^4 slope of the BB curve adjacent to the optically thin CRE calculation at 10^{23} cm^{-3}. Considering that the comparison is between a detailed model of the microprocesses in a plasma and a simple formula describing an ideal radiator, the agreement is significant.

IV. XUV DIAGNOSTICS

The motivation for modeling detailed atomic physics and radiation processes in high-density plasmas is twofold: (1) In medium- to high-Z plasmas, not only is radiation a significant mechanism for the loss and redistribution of plasma energy, but a large proportion of this energy can be contained in ion internal energy. Consequently, the atomic model can seriously affect the partitioning of energy in hydrodynamic calculations. (2) In addition to accurate determination of this partitioning, a detailed atomic model has the added attractiveness of being capable of accurate prediction of the details of emission which can then be used to diagnose conditions in laboratory plasmas. Merging of lines and continuum,[43] as well as line broadening[44] and shift,[45-47] can be helpful in determining plasma densities. Absolute line intensities can be used to predict the approximate size of the emitting region of the plasma. Line intensity ratios[42] are often accurate indicators of both temperature and density. Line ratios have been used extensively in diagnosing the temperature and density of plasmas which emit strongly in the K shell, and many studies[6,8,48-51] have been done to quantify soft x-ray line ratios for this use. Few investigations have dealt, however, with the spectral diagnostics of dense medium- and high-Z plasmas which lie in the XUV region.[52-54] In this section, we investigate several possible line intensity ratios from L-shell aluminum ions that show promise as density and temperature indicators for plasmas typical of exploding wire and laser-created plasma experiments.

A. Temperature determinations

Appropriate line intensity ratios for temperature diagnoses in hot plasmas are relatively abundant in most XUV spectra. Since the ionic populations display the pronounced "picket fence" effect with temperature (as does the ionic radiation, as seen in Fig. 2), intensities of lines from adjacent ions form ratios which are very sensitive to changes in plasma temperature. This would seem to suggest that any number of pairs of lines from adjacent ions are effective diagnostics; in fact, there are further restrictive considerations. In choosing what we consider to be good diagnostics, three additional criteria need to be considered: (1) A good temperature diagnostic line ratio should be comprised of two lines which lie close together in the spectrum. This eliminates many of the experimental uncertainties associated with nonlinear response of crystal or film due to differences in wavelength. (2) The two lines should also be of sufficient intensity to be easily measured and their peak intensities should be comparable, hence, yielding a ratio near 1 in the temperature range of the plasma where the lines are strong emitters. (3) Good temperature diagnostic ratios should be somewhat independent of density variation (over a limited range of interest) and should also exhibit little change due to opacity effects. Of the three conditions, the last is the most difficult to satisfy.

In Table III, selected transition pairs comprising temperature sensitive line intensity ratios for every adjacent pair of L-shell ions are listed which satisfy the first two criteria. Since individual j components of the transitions are not treated in this model, the contributions over a number of wavelengths need to be summed in several cases in order to experimentally obtain the total intensity of the transition as calculated by the model; these wavelengths are also given. The line ratios for these transitions versus electron temperature for an optically thin plasma at 10^{19} ions/cm^3 have been calculated and are shown in Fig. 8. Note that these ratios provide useful diagnosis over a wide range of temperatures corresponding to the range over which L-shell radiation is prominent. In an earlier work[6] on aluminum K-shell diagnostics, it was shown that line intensity ratios formed from lines from heliumlike and hydrogenlike ions provide insight into plasmas temperatures over an effective range beginning at about 300 eV. In light of this result and from examination of Fig. 8, there exists a large temperature range from about 150 eV to about 300 eV in which no temperature diagnostic is available. This is, of course, the range which lies between the lithiumlike and heliumlike systems—the barrier between the two atomic shells. A line ratio was calculated for this pair of ions, but Al XII lines do not effectively turn on until temperatures of about 250–300 eV are reached, resulting in this difficult region for diagnosis. However, this in itself is informative in interpreting spectra. Namely, any time-resolved spectrum in which both lithiumlike and heliumlike lines occur close together in the same wavelength range (for example, 25–50 Å, in aluminum where heliumlike transitions from higher Rydberg states to the $n=2$ levels occur along with lithiumlike transitions from $n \geq 3$ to $n=2$) and show comparable intensities is an indication of a rather *substantial* temperature gradient in the plasma source. This is not necessarily true for lines from adjacent ions *within* the L shell.

The third criteria referred to earlier involves the variation of the temperature-sensitive ratios with density and opacity. If the line ratio varies significantly with either of these plasma parameters, the problem of interpreting the experimental spectrum becomes a very complicated puzzle in which the assessment of size, tem-

TABLE III. Transitions comprising the temperature-sensitive line intensity ratios depicted in Fig. 8.

Key	Ion	Transition	Wavelengths (Å)
III.1	Al IV	$2s^22p^6(^1S)-2s^22p^53d(^3D)$	129.729
	Al V	$2s^22p^5(^2P)-2s2p^4(^3P)3s(^2P)$	130.413, 130.848, 131.003, 131.441
III.2	Al V	$2s^22p^5(^2P)-2s2p^4(^3P)3d(^2D)$	107.945, 108.057, 108.462
	Al VI	$2s^22p^4(^3P)-2s^22p^3(^4S)3s(^3S)$	109.514, 109.843, 109.974
III.3	Al VI	$2s^22p^4(^3P)-2s^22p^3(^4S)3d(^3D)$	92.626, 92.636, 92.875, 92.97
	Al VII	$2s^22p^3(^2P)-2s^22p^2(^1D)3s(^2D)$	90.63
III.4	Al VII	$2s^22p^3(^4S)-2s^22p^2(^3P)3d(^4P)$	75.27, 75.320, 75.36
	Al VIII	$2s2p^3(^3D)-2s2p^2(^2D)3s(^3D)$	75.577
III.5	Al VIII	$2s2p^3(^5S)-2s2p^2(^4P)3d(^5P)$	66.704, 66.731, 66.771
	Al IX	$2s^22p(^2P)-2s^23s(^2S)$	66.624, 66.836
III.6	Al IX	$2s2p^2(^4P)-2s2p3d(^4D)$	60.504, 60.549, 60.588, 60.645
	Al X	$2s2p(^1P)-2s3d(^1D)$	59.107
III.7	Al X	$2s^2(^1S)-2s3p(^1P)$	51.979
	Al XI	$2p(^2P)-3s(^2S)$	54.39

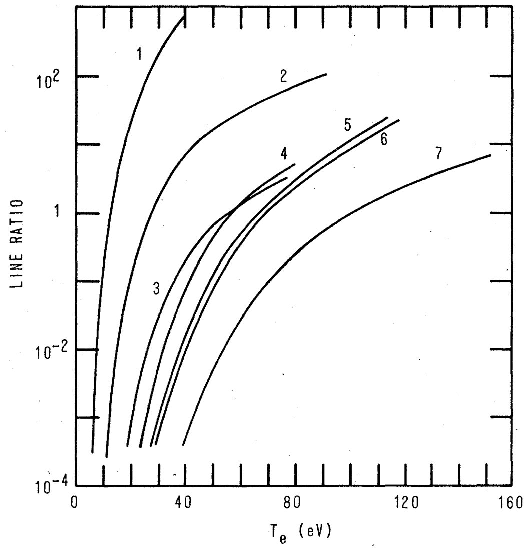

FIG. 8. Temperature-sensitive line intensity ratios for selected L-shell lines at 10^{19} ions/cm^3 (optically thin approximation). (See Table III for key.)

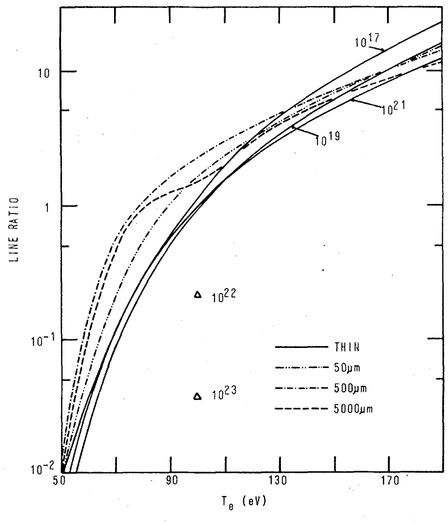

FIG. 9. Line intensity ratio for the $2p$–$3s/2s^2$–$2s3p$ (^1P) transitions for densities of 10^{17}, 10^{19}, and 10^{21} ions/cm^3 (optically thin approximation) and for a plasma cylinder at 10^{19} ions/cm^3 (with opacity effects) for radii of 50–5000 μm.

perature, and density are all strongly coupled. In order to illustrate these effects on the line ratios listed in Table III, the $2p$–$3s/2s^2$–$2s3p(^1P)$ ratio (III.7, see Table III) was selected as an example. This ratio was calculated from 50 to 200 eV for plasmas of 10^{17}, 10^{19}, and 10^{21} ions/cm^3 in the optically thin approximation and at 10^{19} ions/cm^3 with opacity effects for plasma of radii 50, 500, and 5000 μm; the results are displayed in Fig. 9. The results show primarily, that the line intensity ratio depends only slightly on the plasma density between 10^{17} and 10^{21} ions/cm^3. The ratio tends to diverge more as the temperature increases, so that at 170 eV, near the upper temperature limit for applicability of this diagnostic (the Al X line is too faint above this temperature), the ratio at 10^{17} cm^{-3} is about 1.6 times the ratio at 10^{21} cm^{-3}. If one were to use the low-density curve as a universal one, and attempt to diagnose a high-density plasma, errors in the predicted temperature of 25–30 eV could be expected. In reality, the density is usually known to within an order of magnitude, and using the results of this model, one could anticipate only small discrepancies in a temperature determination using this ratio. Nevertheless, the density effects on the ratio are so small within the range of Fig. 9, that practically speaking, the ratio is density insensitive. The reason for this insensitivity is not immediately apparent. Close inspection of the dominant depopulating rates of the upper levels of each transition shows that over the 4 orders of magnitude change in density in Fig. 9, the levels traverse from the coronal region to the collision-dominated plasma regime. The radiative decay coefficients for the $2p$–$3s$ and $2s^2$–$2s3p$ transitions are 1.5×10^{11} and 4.6×10^{11} sec^{-1}, respectively. At 10^{17} ions/cm^3 and 100 eV, the respective electron collisional deexcitation rates are 5.3×10^8 and 2.8×10^8 cm^3/sec, well below the radiative decay rates, implying a coronal behavior for the upper-level populations. Thus, the line intensities are given approximately by

$$I = N_u A \Delta E = N_l X N_e \Delta E\,, \tag{11}$$

where u and l denote upper and lower states of the transition. Hence, at constant temperature, each line intensity scales as the total ion density squared, and the line ratio remains *constant* at coronal densities. At 10^{21} ions/cm^3, however, the collisional deexcitation rates are 5.3×10^{12} and 2.8×10^{12} cm^3/sec, exceeding the radiative decay rates by factors of 35 and 6, respectively. At this density, the L-shell ion populations are approaching their LTE distribution. In LTE, we can relate the $2s3p\,^1P$ state population (N_1) to the $2s\,^2S$ ground state population (N_0) by the Saha equation,

$$\frac{N_e N_0}{N_1} = \frac{g_0}{g_1}\,\frac{2(2\pi mkT)^{3/2}}{h^3}\exp\left(\frac{-\Delta E_{10}}{T}\right). \tag{12}$$

We can also express the relationship between the $2s$ and $3d$ (N_2) levels of Al XI via Boltzmann's law,

$$\frac{N_2}{N_0} = \frac{g_2}{g_0}\exp\left(\frac{-\Delta E_{02}}{T}\right). \tag{13}$$

Eliminating N_0 and g_0, we find,

$$\frac{N_2}{N_1} = \frac{g_2}{N_e g_1} \frac{2(2\pi mkT)^{3/2}}{h^3} \exp\left(\frac{-\Delta E_{12}}{T}\right) . \tag{14}$$

Thus, in strict LTE, the ratio of the populations and, hence, the line intensities (in the optically thin approximation) scale by a factor of N_e^{-1}. To illustrate, we have plotted, as isolated points, the line ratio at densities of 10^{22} and 10^{23} ions/cm^3 and a temperature of 100 eV in Fig. 9. It becomes apparent that this line ratio loses its "density insensitive" quality somewhere between 10^{21} and 10^{22} ions/cm^3 as the levels make the transition from the collisional-radiative regime to that of LTE. In fact, this is the criteria which determines the density sensitivity of the other line intensity ratios in Table III; as two adjacent ions approach a state of LTE, the line ratio formed by emission lines from each of them becomes very dependent on the plasma density and unsuitable as a temperature diagnostic unless the density is known to good accuracy.

The effect of photoexcitation on the line ratio is also shown in Fig. 9. As the temperature increases, it is generally the transition from the lower-charge ion which first becomes attenuated by the plasma opacity, causing an initial increase in the value of the line ratio compared to the optically thin value. As the temperature continues to increase, the ionic populations change and the transition from the higher-charge ion becomes optically thick, reducing the ratio somewhat as compared to the thin value; both of these effects are seen in Fig. 9. Notice that the larger 5000-μm plasma exhibits a ratio closer to the thin values than the 500-μm plasma from about 50 to 150 eV. This is a function of the relative values of oscillator strengths and collisional quenching rates of the respective transitions. This behavior, therefore, is particular to these transitions at this density, and is not characteristic of any general trend in radiation transport effects. The absence of radiation transport can lead to errors in the calculation, as seen in Fig. 9, but these errors would lead to temperatures which are typically 10 to 20 eV higher than the correct calculation yields. At lower densities, the tendency toward an optically thin plasma reduces these effects somewhat. The way to reduce opacity effects in line intensity ratios is (1) to choose transitions which have small oscillator strengths, or (2) which end on levels which are not as highly populated as the ground state. Unfortunately, this results, in the first case, in choosing transitions which may be too weak to detect. The second case is not useful since the *L*-shell excited-state populations are not significantly smaller than the ground states in the density regime of interest for this investigation. Hence, if a truly accurate determination is required, a detailed calculation with radiation transport is necessary.

B. Density determinations

The criteria discussed in the previous section concerning good temperature diagnostic line ratios apply to good density diagnostic line ratios by simply interchanging the words temperature and density. Density diagnostics, however, were much more difficult to locate in the spectrum since the variation of line intensities with density is not as straightforward as it is with temperature. In addition, several of the diagnostic ratios first selected, although density sensitive, displayed only small changes in the value of the line ratio with density variations; thus, experimental error would introduce large uncertainties in density determinations. We found we were most successful by choosing lines which originated from different spin systems within the same ion. Because of the forbidden nature of the transitions of different spin-system levels to the ground state, density effects were often profound in determining the population of the excited states. Lines from the same ion were chosen to ensure that the radiation from both lines was emitted from the same location in the plasma. A problem which occurs in these diagnostics for *L*-shell ions is the narrow range of temperatures over which the ions exist (see Fig. 2). As the plasma temperature deviates slightly from the small interval over which the transitions radiate strongly, the line ratios become extremely temperature dependent. Three pairs of lines were selected as density diagnostics over a limited range of temperatures, however, and they are listed in Table IV along with the relevant wavelengths. The line intensity ratios for these transitions are plotted vs. ion density in Figs. 10–12 for an optically thin plasma for several electron temperatures at which the lines are strong radiaters. In Fig. 10, the two transitions are from nitrogenlike Al VII; from Fig. 2, the line emission from this ion peaks at about 35 eV and the line ratio at 30 and 40 eV in Fig. 10 are reasonably close above 3×10^{18} ions/cm^3. The ratio at 50 eV displays larger deviations from the other curves above this density, since the Al VII emission is already 15 eV removed from the peak emitting temperature. Note also the double valuedness of the ratio complicates spectral interpretation even further. This ratio is typical of the transition pairs we investigated from Al IV–Al VII ions; significant temperature de-

TABLE IV. Transitions comprising the density-sensitive line intensity ratios depicted in Figs. 10–12.

Ion	Transition	Wavelengths (Å)
Al VII	$2s^22p^3(^4S)-2s^22p^23s(^4P)$	86.887, 87.06, 87.176
Al VII	$2s^22p^3(^2D)-2s^22p^2(^1D)3s(^2D)$	88.033
Al VIII	$2s^22p^2(^3P)-2s^22p3d(^3D)$	67.36, 67.408, 67.437, 67.464, 67.529
Al VIII	$2s2p^3(^5S)-2s2p^23d(^5P)$	66.704, 66.731, 66.771
Al X	$2s2p(^1P)-2s3d(^1D)$	59.107
Al X	$2s2p(^3P)-2s3d(^3D)$	55.227, 55.272, 55.376

pendence over even small ranges of T_e. In Figs. 11 and 12, the line ratios show much less temperature sensitivity and no double valuedness in the useful density region. In Fig. 12, the ratio changes very little over a temperature range of 80 eV, causing, for example, an error of at most a factor of 5 in the density determination if the experimental line ratio was 2.0. It is assumed, however, that the temperature could be determined to better accuracy than that from diagnostics presented earlier, and the density could probably be determined to less than a factor of 2 error by a comprehensive analysis of the spectrum. Agreement between many aspects of the theoretical and experimental spectrum is in fact the only way to insure that the plasma has been accurately characterized by the model. In the following section, this point is explored in relation to the generation of theoretical spectra with CRE calculations.

V. CALCULATION OF THEORETICAL SPECTRA

In the previous sections, we presented the results of L-shell aluminum calculations which we deemed useful in gaining understanding of the radiation energetics in dense plasmas over a wide range of temperatures, as well as providing diagnostic information applicable to the determination of plasma parameters. Although one can often make a strong case for an attempt to characterize a plasma via an isolated diagnostic, we are of the opinion that ionization-radiation dynamic calculations have, at present, reached a level of sophistication that allows for direct comparisons of theoretically generated spectra and those obtained experimentally. Moreover, it is our contention that only by this comprehensive replication of line and continuum radiation signatures, that anything definitive can be said about the ability of the theoretical calculations to characterize the experimental plasma. In this section, theoretical spectra calculated by our radiation model for a plasma with a temperature gradient similar to that found in imploding wire array plasmas are presented and discussed. These spectra are not intended to be an attempt to model any individual wire implosion but are meant to be illustrative of the ability of the theoretical model to produce spectra suitable for

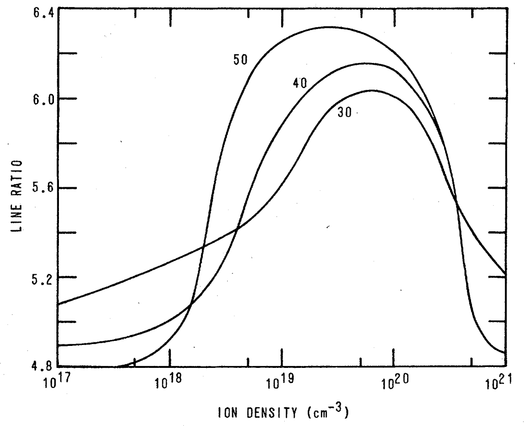

FIG. 10. Line intensity ratio for the $2s2p(^1P)-2s3d(^1D)/2s2p(^3P)-2s3d(^3D)$ transitions vs ion density, for several electron temperatures (optically thin approximation).

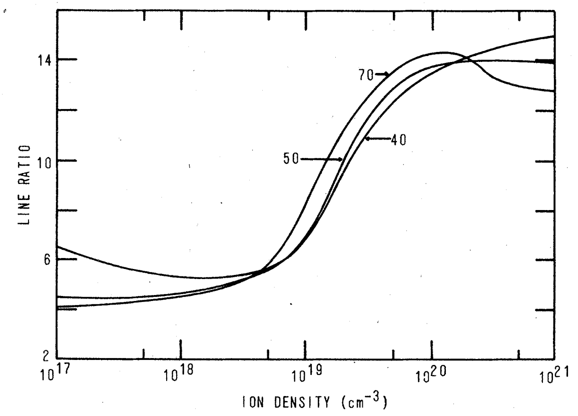

FIG. 11. Line intensity ratio for the $2s^22p^2(^3P)-2s^22p3d(^3D)/2s2p^3(^5S)-2s2p^23d(^5P)$ transitions vs ion density, for several electron temperatures (optically thin approximation).

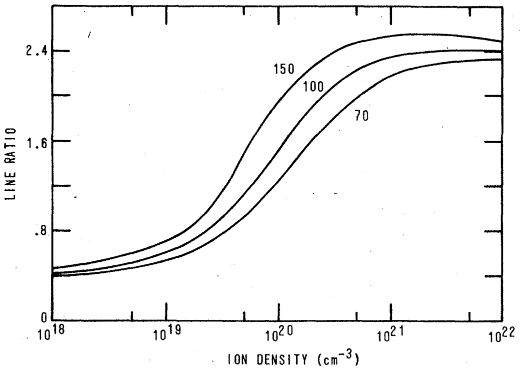

FIG. 12. Line intensity ratio for the $2s^22p^3(^4S)-2s^22p^23s(^4P)/2s^22p^3(^2D)-2s^22p^2(^1D)3s(^2D)$ transitions vs ion density, for several electron temperatures (optically thin approximation).

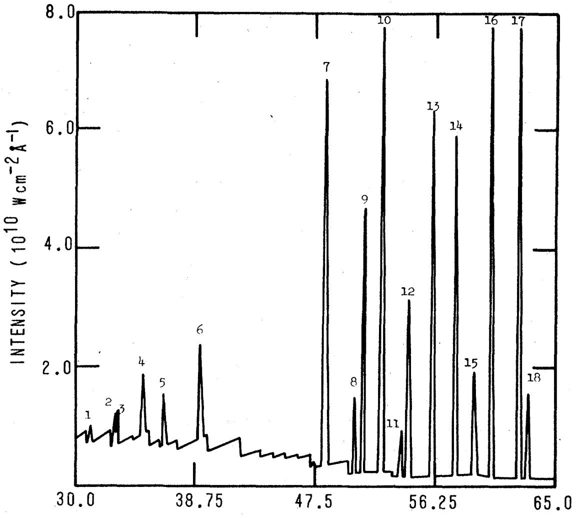

FIG. 13. Aluminum spectrum from 30–65 Å for a plasma at 10^{19} ions/cm^3 and a linear temperature gradient from 30 to 80 eV.

comparison with experiment using only plasma temperature, density, and size of emitting region as input parameters. For examples of actual experimental spectra from imploding wire plasmas and other dense plasma sources, the reader is referred to an upcoming paper by Nagel.[13]

Within the probability of escape phenomenology employed by this model, a radiation spectrum can be calculated by summing the frequency-by-frequency contributions from each plasma zone for line emission, recombination radiation, and bremsstrahlung. Only the bremsstrahlung is not transported through the plasma since the free-free opacity is small for the density and temperature regime of interest here. The contribution from each zone is determined from the radiative source function and the probability of escape to the vacuum region beyond the outer boundary of the plasma. This zone-by-zone treatment produces a spectrum in which lines are superpositions of a number of different profiles and the continuum is a superposition of a number of different slopes, depending on the zonally determined temperature and density as well as the transport-dependent atomic state population densities. The results are displayed as spectral intensity (in $W cm^{-2} Å^{-1}$) radiated into 4π radians and plotted versus wavelength.

The temperature gradient for this example was chosen so as to approximately describe an imploded cylindrical aluminum plasma which is assembled on axis and is at the point of maximum emission in its time evolution. The plasma is taken to be 1 mm in diameter with a linear temperature gradient from 80 eV in the central region to 30 eV near the periphery. A hot K-line emitting core is usually present in these plasmas but was neglected here since it is our purpose to illustrate the emission solely from the L-shell lines in this study; however, the K lines are easily included in the calculation by altering the temperature profile to reflect K-shell emission temperatures. A comparison of theoretical and experimental spectra from aluminum K-shell ions is the subject of another study.[55] Although a density gradient most likely exists in actual imploded plasmas, none was included in this example in order to eliminate confusion over which effects are due to a temperature gradient and which are due to a density profile. Moreover, a temperature profile alone is sufficient to illustrate the varied line emission from the L-shell ions as would be recorded by a spectrometer for an actual experiment.

The calculated theoretical spectra for the above conditions are reproduced in Figs. 13–15. Approximately 30 mÅ of source and instrumental broadening has been convoluted with the line profiles to duplicate similar conditions as would be present in experimental spectra, since this broadening mechanism often dominates line profiles for plasmas of these temperatures and densities. In Figs. 13 and 14, the spectral intensity has been plotted on a linear y axis as would an experimental spectrum; the wavelength range has been separated into the 30–65-Å and 65–105-Å regions in order to show better detail. The 30-Å cutoff just includes the Al XI $2s-6p$ line, the shortest wavelength line in our L-shell model (excluding the satellite line from the doubly excited $1s2p^2\,^2D$ state). If K-shell emission intensity had been comparable to the L-shell

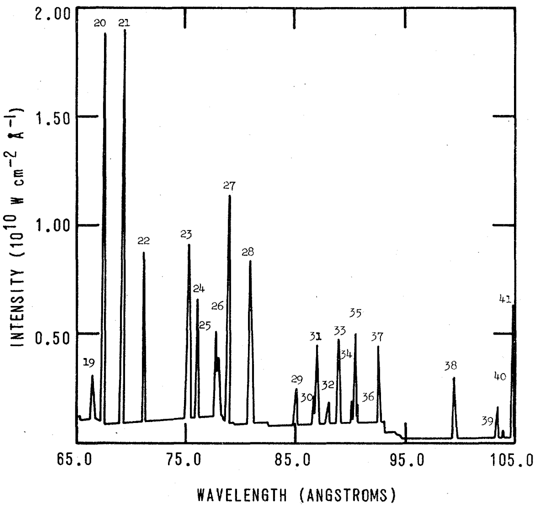

FIG. 14. Aluminum spectrum from 65–105 Å for a plasma at 10^{19} ions/cm^3 and a linear temperature gradient from 30 to 80 eV.

lines, however, several Balmer series lines from the hydrogenlike and heliumlike ions could be seen among the L-shell lines ranging from about 25 to 52 Å. Notice that we have allowed several very prominent lines to "saturate" our theoretical "spectrometer film" in order to display some of the lower intensity lines of the spectra. The jagged base line is due to recombination edges forming the free-bound continuum (the bremsstrahlung is very much lower); in actual experimental spectra, the noise level often washes out much of the finer detail of this feature, while the absorption edges of filters frequently distort the true shape of this emission profile. Identification of the individual lines is accomplished by numbering in order of increasing wavelength, with Table V serving as a key; also given in Table V is the transition wavelength and the optical depth at line center, calculated from the central axis of the plasma to the outer boundary. The wavelengths quoted in this table are, in some cases, averages over a number of transitions

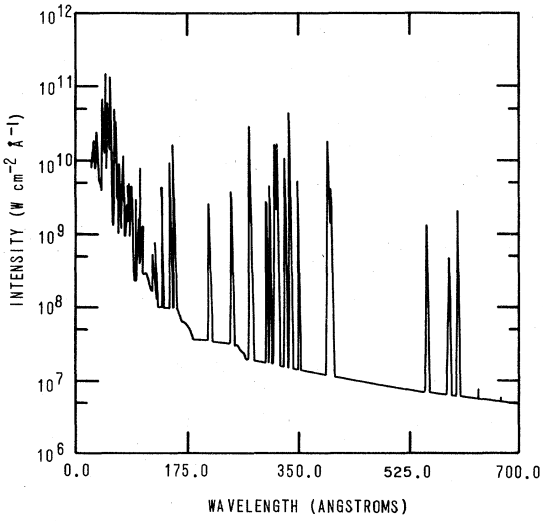

FIG. 15. Aluminum spectrum from 0–700 Å for a plasma at 10^{19} ions/cm^3 and a linear temperature gradient from 30 to 80 eV.

TABLE V. Transitions shown in the spectral plots, Figs. 13 and 14 with their wavelengths (note: wavelengths may be averaged over several transitions within the same configuration), and their line-center optical depths measured from plasma center for the conditions described in Sec. V.

Key		Transition	Wavelength (Å)	τ_o
V.1	Al XI	$2s-6p$	31.31	7.3
V.2	Al XI	$2s-5p$	33.007	14.7
V.3	Al XI	$2p-6s,-6d$	33.109	20.4
V.4	Al XI	$2p-5s,-5d$	34.994	44.0
V.5	Al XI	$2s-4p$	36.675	38.5
V.6	Al XI	$2p-4s,-4d$	39.28	132.6
V.7	Al XI	$2s-3p$	48.297	193.2
V.8	Al X	$2s2p-2p3p$	50.47	70.2
V.9	Al X	$2s^2-2s3p$	51.096	147.1
V.10	Al XI	$2p-3d$	52.299	937.2
V.11	Al X	$2s2p-2p3p$	53.83	25.3
V.12	Al XI	$2p-3s$	54.388	31.1
V.13	Al X	$2s2p-3s,-3d$	56.06	195.4
V.14	Al X	$2p^2-2p3s,-3d$	57.74	418.0
V.15	Al X	$2p^2-2p3s,-3d$	59.1	157.3
V.16	Al X	$2s2p-2s3d,-3s$	60.36	353.8
V.17	Al IX	$2p-3s,-3d$	62.37	786.6
V.18	Al IX	$2s2p^2-2s2p3d$	62.97	206.7
V.19	Al VIII	$2s2p^3-2s2p^23d$	66.72	47.7
V.10	Al VIII	$2p^2-2p3d$	67.62	995.0
V.21	Al VIII	$2p^2-2p3d$	69.36	560.0
V.22	Al VIII	$2s2p^3-2s2p^23d$	71.27	191.1
V.23	Al VII	$2p^3-2p^23d$	75.32	647.4
V.24	Al VII	$2p^3-2p^23d$	76.17	406.0
V.25	Al VIII	$2s2p^3-2s2p^23s$	77.92	44.4
V.26	Al VII	$2p^3-2p^23d$	78.10	116.8
V.27	Al VII	$2p^3-2p^23d$	78.93	61.5
V.28	Al VII	$2p^3-2p^23d$	81.02	338.1
V.29	Al XI	$3s-6p$	85.19	0.9
V.30	Al VI	$2p^4-2p^33d$	86.84	102.1
V.31	Al VII	$2p^3-2p^23s$	87.07	94.0
V.32	Al VII	$2p^3-2p^23s$	88.04	19.1
V.33	Al XI	$3p-6s,-6d$	88.99	3.5
V.34	Al VI	$2p^4-2p^33d$	90.19	54.3
V.35	Al XI	$3d-6p,-6f$	90.44	5.1
V.36	Al VII	$2p^3-2p^23s$	90.64	6.9
V.37	Al VI	$2p^4-2p^33d$	92.65	260.3
V.38	Al XI	$3s-5p$	99.59	2.4
V.39	Al VI	$2p^4-2p^33s$	103.46	57.7
V.40	Al V	$2p^5-2p^43d$	103.92	7.00
V.41	Al XI	$3p-5s,-5d$	104.82	10.1

with similar initial and final electron configurations but different angular momentum states; hence, they may not correspond exactly to values quoted by standard references for a given transition.

From Fig. 13, it is seen that the strongest emitters in this plasma are the lithiumlike $2p$–$3d$ transition (V. 10, see Table V), the berylliumlike $2s2p$–$2s3d$, –$3s$ (singlet) transitions (V. 16), and the boronlike $2p$–$3d$, –$3s$ (doublet) transitions (V. 17). For the latter two lines, the intensity is due almost entirely to the transitions from the $3d$ levels, since both the population of these states and radiative decay rates from them exceed those of the corresponding $3s$ levels. An interesting feature that became apparent when comparisons were made with experimental spectra was the relative heights of the Al XI $2s$–$5p$ (V. 2) and $2p$–$6d$, –$6s$ (V. 3) lines. In all spectra examined, the shorter wavelength line always exceeded the longer one in intensity. Yet, when optically thin calculations were analyzed, the longer wavelength line dominated at all temperatures and over a wide range of densities. It was only when opacity effects were included in the analysis that the emission lines reversed their relative intensities and agreed with experimental data. The phenomenon is explained by the larger optical depth of the $2p$–$6d$ line; since both the $2s$–$5p$ and $2p$–$6d$ oscillator strengths are comparable (about a 2:3 ratio), the difference in opacity lies with the population density of the lower state of the transition. At these densities, the $2s$ and $2p$ levels are populated approximately according to their statistical weights at temperatures where Al XI lines emit strongly. Consequently, the $2p$–$6d$ optical depth will be about 2 to 3 times larger than that of the $2s$–$5p$ transition and the former line will be attenuated more as the plasma becomes increasingly optically dense. Initially, it was thought that this feature could be useful as an opacity diagnostic to estimate the size of the emitting region; however, the relative changes in intensities of the two lines with plasma size was found to be too small to derive sufficiently accurate quantitative information to be able to make a definitive statement about this plasma parameter.

In Fig. 14, lines from the lower ionization stages are prevalent, with Al VI–Al VIII dominating the emission. The lines from Al III–Al V do not appear with sufficient intensity to be seen since these ions are dominant at temperatures lower than the 30-eV cutoff in our profile used in this example. In fact, this lower limit on the temperature gradient was chosen after several examples of data from aluminum wire experiments were scanned and few intense contributions to the line spectrum from these ions found.

In order to illustrate the gross characteristics of the radiation spectrum from this sample run, Fig. 15 was plotted with a logarithmic y axis, exhibiting low intensitity lines as well as the stronger ones. At the longer wavelengths, above about 240 Å, lines due to $\Delta n = 0$ transitions among the $n = 2$ levels of the L-shell ions are prominent along with a few weak lines from higher Rydberg state transitions in Al XI. The real value of a comprehensive spectrum as shown in Fig. 15 is in its ability to indicate, at a glance, which wavelength regions are responsible for the bulk of the emission. In particular, the wavelength dependence of the free-bound continuum radiation, which was seen from Fig. 6 to constitute a significant fraction of the total emission, is very clearly illustrated. This extensive picture of the radiation emission as a function of wavelength is extremely useful when knowledge of the emission from particular "energy bins" is required. In particular, single-temperature analytic models of the plasma dynamics often characterize the plasma radiation in a very approximate way, such as assuming that all the line emission is radiated at a single frequency and an appropriate optical depth, in attempt to mock up, in a concise manner, the actual emission energetics while taking some opacity effect into account. Based on runs made with a flat temperature profile, we find that comprehensive spectral plots display even more localized emission than is shown in Fig. 15 for the exemplary temperature profile. Thus, these plots serve to quantify the overall plasma emission in a way that may easily be implemented in a simple analytic calculation.

Although qualitative comparisons have been made using the spectra generated by this model and a few random experimental spectra, no attempt has, as yet, been made to quantitatively compare the theory with a specific experiment in order to diagnose the plasma conditions at the time of emission. Recently, however, spectroscopists at many laboratories have realized the wealth of information contained in the XUV region of the emission spectrum from dense plasmas, and have begun to make serious attempts to obtain good spectral data in that wavelength range as well as in the soft x-ray region dominated by the K-shell lines. It is our hope that through direct comparison of theoretical and experimental data, this model may make adequate use of that information and shed light on the continuing problem of the characterization of dense plasma dynamics and the determination of basic plasma parameters.

ACKNOWLEDGMENTS

The authors would like to thank M. Blaha, P. C. Kepple, and V. L. Jacobs for many helpful suggestions regarding the detailed atomic physics, and M. Davis, J. Cain, and R. Ernst for their assistance in organizing the enormous data base used in these calculations. This work was supported by the Defense Nuclear Agency.

---

[1] P. G. Burkhalter, C. M. Dozier, and D. J. Nagel, Phys. Rev. A 15, 700 (1977).

[2] P. Burkhalter, J. Davis, J. Rauch, W. Clark, G. Dahlbacka, and R. Schneider, J. Appl. Phys. 50, 705 (1979).

[3] I. Yu. Skobelev, A. V. Vinogradov, and E. A. Yukov, Phys. Scr. 18, 78 (1978).

[4] L. E. Chase, W. C. Jordan, J. D. Perez, and J. G. Pronko, Appl. Phys. Lett. 30, 137 (1977).

[5] D. J. Johnson, G. W. Kuswa, A. V. Farnsworth, Jr., J. P. Quintenz, R. J. Leeper, E. J. T. Burns, and S. Humphries, Jr., Phys. Rev. Lett. 42, 610 (1979).

[6] D. Duston and J. Davis, Phys. Rev. A 21, 1664 (1980).

[7] D. Duston and J. J. Duderstadt, Phys. Rev. A 18, 1707 (1978).

[8] Jon C. Weisheit, C. Bruce Tartar, James H. Scofield, and Leland M. Richards, J. Quant. Spectros. Radiat. Transfer, 16, 659 (1976).

[9] R. K. Landshoff and J. D. Perez, Phys. Rev. A 13, 1619 (1976).

[10] A. L. Hoffman and E. A. Crawford, J. Appl. Phys. 49, 3219 (1978); D. Salzmann and A. Krumbein, *ibid.* 49, 3229 (1978).

[11] J. D. Perez and Gerald L. Payne, Phys. Rev. A 21, 969 (1980); G. A. Doschek and U. Feldman, NRL Memorandum Report No. 8416, 1980 (unpublished).

[12] F. M. Bacon and H. A. Watts, J. Appl. Phys. 46, 4758 (1975).

[13] D. J. Nagel (unpublished).

[14] S. Bashkin and J. O. Stoner, Jr., *Atomic Energy Levels and Grotrian Diagrams* (North-Holland, Amsterdam, 1975), Vol. 1.

[15] W. C. Martin and Romuald Zalubas, J. Phys. Chem. Ref. Data 8, 817 (1979).

[16] R. L. Kelly and L. J. Palumbo, *Atomic and Ionic Emission Lines Below 2000 Angstroms* (U.S. GPO, Washington, D.C., 1973).

[17] D. Duston, J. Davis, and K. G. Whitney, NRL Memorandum Report No. 3846, 1978 (unpublished).

[18] K. G. Whitney and J. Davis, J. Appl. Phys. 45, 5294 (1974); J. Davis and K. G. Whitney, *ibid.* 47, 1426 (1976).

[19] M. J. Seaton, Proc. Phys. Soc. London 79, 1105 (1962).

[20] V. L. Jacobs, J. Davis, P. C. Kepple, and M. Blaha, Astrophys. J. 211, 605 (1977).

[21] W. J. Karzas and B. Latter, Astrophys. J. Suppl. Ser. 6, 167 (1961).

[22] V. L. Jacobs and J. Davis, Phys. Rev. A 18, 697 (1978).

[23] L. A. Vainshtein and I. I. Sobel'man, Lebedev Report No. 66, 1967 (unpublished).

[24] J. Davis, P. C. Kepple, and M. Blaha, J. Quant. Spectrosc. Radiat. Transfer 16, 1043 (1976).

[25] E. Oran and J. Davis, J. Appl. Phys. 45, 2480 (1974).

[26] J. Davis, J. Quant. Spectrosc. Radiat. Transfer 14, 549 (1974).

[27] D. R. Bates and A. Damgaard, Philos. Trans. R. Soc. London Ser. A 242, 101 (1949).

[28] A. Lindgård and S. E. Nielsen, At. Data Nucl. Data Tables 19, 533 (1977).

[29] B. C. Fawcett, At. Data Nucl. Data Tables 22, 473 (1978).

[30] I. Martin and G. Simons, Mol. Phys. 32, 1017 (1976).

[31] L. J. Shamey, J. Opt. Soc. Am. 61, 942 (1971).

[32] A. W. Weiss, Phys. Rev. A 188, 119 (1969).

[33] L. C. McIntyre, Jr., D. J. Donahue, and E. M. Bernstein, Phys. Scr. 17, 5 (1977).

[34] J. P. Buchet and M. C. Buchet-Poulizac, Phys. Lett. 63A, 267 (1977).

[35] J. A. Kernahan, E. H. Pinnington, J. A. O'Neill, R. L. Brooks, and K. E. Donnelly, Phys. Scr. 19, 267 (1979).

[36] R. Mewe, Astron. Astrophys. 59, 275 (1977).

[37] P. Shorer, Phys. Rev. A 20, 642 (1979).

[38] A. V. Loginov and P. F. Gruzdev, Opt. Spektrosk. 45, 839 (1978) [Opt. Spectrosc. (USSR) 45, (5), 725 (1978)].

[39] W. Wiese, M. Smith, and B. Miles, *Atomic Transition Probabilities* (U.S. GPO, Washington, D.C., 1969), Vol. II.

[40] D. G. Hummer, Astrophys. J. 140, 276 (1964).

[41] J. P. Apruzese, J. Davis, D. Duston, and K. G. Whitney, J. Quant. Spectrosc. Radiat. Transfer 23, 479 (1980).

[42] Hans R. Griem, *Plasma Spectroscopy* (McGraw-Hill, New York, 1964).

[43] J. Davis, NRL Memorandum Report No. 2655, 1973 (unpublished).

[44] H. R. Griem, M. Blaha, and P. C. Kepple, Phys. Rev. A 19, 2421 (1979).

[45] H. R. Griem, *Spectral Line Broadening by Plasmas* (Academic, New York, 1974).

[46] J. C. Weisheit and B. F. Rozsnyai, J. Phys. B 9, L63 (1976).

[47] Stanley Skupsky, Phys. Rev. A 21, 1316 (1980).

[48] A. V. Vinogradov, I. Yu. Skobelev, and E. A. Yukov, Kvant. Elektron. (Moscow) 2, 1165 (1975) [Sov. J. Quant. Electron 5, 630 (1975)]; Zh. Eksp. Teor. Fiz. 72, 1762 (1977) [Sov. Phys.—JETP 45, 925 (1977)].

[49] U. Feldman, G. A. Doschek, D. K. Prinz, and D. Nagel, J. Appl. Phys. 47, 1341 (1976).

[50] C. P. Bhalla, A. H. Gabriel, and L. P. Presnyakov, Mon. Not. R. Astron. Soc. 172, 359 (1975).

[51] H. J. Kunze, A. H. Gabriel, and H. R. Griem, Phys. Rev. 165, 267 (1968).

[52] G. V. Peregudov, E. N. Ragozine, I. Yu. Skobelev, A. V. Vinogradov, and E. A. Yukov, J. Phys. D 11, 2305 (1978).

[53] V. A. Boiko, A. Yu. Chugunov, T. G. Ivanova, A. Ya. Faenov, I. V. Holin, S. A. Pikuz, A. M. Urnov, L. A. Vainshtein, and U. I. Safronova, Mon. Not. R. Astr. Soc. 185, 305 (1978).

[54] N. A. Ebrahim, M. C. Richardson, G. A. Doschek, and U. Feldman, J. Appl. Phys. 51, 182 (1980).

[55] P. G. Burkhalter, D. Duston, and J. Davis (unpublished).